RESEARCH ARTICLE

RHM-δ-GLMB Tracking Algorithm on the Focal Plane for UAV Cluster Targets

YIJIN WANG[1], **CHUANGMING TONG**[1], **AND JIAHAO XIE**[2]

[1]Air and Missile Defense College, Air Force Engineering University, Xi'an 710051, China
[2]Space Engineering University, Beijing 101416, China

Corresponding author: Jiahao Xie (18222517021@163.com)

ABSTRACT This paper offers a new tracking algorithm for clustered targets of focal plane unmanned aerial vehicles (UAVs) by integrating the random hypersurface model (RHM) model into the δ-generalized label multi-Bernoulli (δ-GLMB) filter to guarantee a robust UAV cluster target tracking on such focal planes. We first investigated the infrared imaging features of UAV cluster targets by emphasizing the target imaging size and dispersion. Next, we designed an elliptical RHM-based measurement model to map the measurement, state parameters, scaling factors, and errors to pseudo-measurement "0", followed by establishing a pseudo-measurement equation to reflect the target's extended shape size. Then, in order to enhance measurement estimation accuracy, the RHM model was implemented with the δ-GLMB filter and Gamma-Gaussian mixture, which can perform a real-time estimate of the targets' centroid motion state and extended state. We also used the grid-based fast density-based spatial clustering of applications with noise (DBSCAN) segmentation algorithm to overcome the distance-based segmentation method restrictions for infrared radiation (IR) measurement data and diminish the algorithm's complexity even more in the measurement update. Extensive simulations demonstrated that this algorithm outperformed existing matching filtering algorithms in the target centroid motion and extended states. Our investigations also revealed that the algorithm was less vulnerable to clutter and more adaptive, making it more straightforward to accomplish reliable tracking of UAV cluster targets.

INDEX TERMS UAV cluster, RHM model, extended multi-target tracking, δ-GLMB filter, OSPA distance.

I. INTRODUCTION

Multi-target filtering is the sequential estimation of a target's current state that may emerge, move and disappear, given previous and current noise sensor data. It is widely utilized in military and civilian applications, including air traffic control [1], [2], ship tracking at sea [3], and autonomous driving [4]. A cluster target is a group of spatially confined targets that move collaboratively, such as unmanned aerial vehicle (UAV) clusters, convoys, and bird flocks [5]. They may be perceived as formations of cooperating individuals whose locations obey a particular structure. Accordingly, this paper concentrates on tracking UAV cluster targets.

Traditional multi-target tracking algorithms represent targets as point targets and presume that a single-point

The associate editor coordinating the review of this manuscript and approving it for publication was Chengpeng Hao.

target provides only one measurement, following the combination of targets and measures to track multiple targets. Reference [6] proposed a flexible and effective tracker that divided the tracking task into classification and regression. To comprehensively use the local and context information, [7] depicted the Siamese Parallel Interaction Network tracker. However, the data correlation between measurements and targets frequently results in a computational load that is exceptionally challenging for these algorithms. In such cases, although the distance between the measurements generated by individual population targets is small compared to the detection gate, making it challenging to estimate the target states, the population's targets are spread near enough, or the sensors far enough away from the targets. Thus, estimating the group targets' extended state and measurement rate to assess the kinematic state of group targets, as in standard point target tracking, has been proposed.

Accordingly, Mahler implemented a probabilistic hypothesis density (PHD) filter [8] based on the finite set statistics theory (FISST) [9] to handle this problem. Examples of highly sophisticated FISST algorithms are the Cardinalized PHD (CPHD) filter, the Cardinal Balanced Multi-target Multi-Bernoulli (CBMeMBer) filter, and the generalized label multi-Bernoulli (GLMB) filter [10], [11], [12]. Consequently, their study tracked an unknown number of multiple targets in Poisson false alarms, missed detections, and target emergence, disappearance, and generation.

In a previous study, B. T. Vo et al. [13] demonstrated the δ-generalized label multi-Bernoulli (δ-GLMB) filter. Since the δ-GLMB filter is based on the GLMB density relative to the multi-target measurement probability and is closed under the Chapman-Kolmogorov prediction equation, it could model target states using labeled random finite sets (RFS), allowing the target state to span several time steps and enabling trajectory generation. Reference [14] also describes a computationally efficient version of the δ-GLMB filter that integrates prediction and updates it into a single phase. The label multi-Bernoulli (LMB) filter and the marginalized δ-GLMB filter are emphasized as principle approximations of the δ-GLMB filter that retain the essential statistical aspects of the total multi-target density. The states and measurements of the targets are modeled using random finite sets (RFS) in these filter algorithms, as mentioned earlier, eliminating the computational complexity of data correlation. Reference [15] applies the δ-GLMB filter to track UAV cluster targets, concentrating on three distinct views to simulate and investigate the tracking problem during UAV cluster splitting and merging. Due to the loss of extended information, however, the previously mentioned extended target tracking filter algorithms can only approximate the kinematic state of the target centroid, resulting in tracking errors.

Despite the successes of the above studies, it remains problematic to generate stable trajectories for dense targets with low measurement precision and significant echo crossover. Therefore, a holistic tracking strategy has been recommended to focus on the group shape and centroid state rather than the targets inside the group. For instance, [16] highlighted a random matrix method to estimate the kinematic and extended states simultaneously, characterizing the group's center of mass variation by the kinematic model and the group's extended state variation by the random matrix. Other studies then cultivated the Gaussian inverse Wishart probability hypothesis density (GIW-PHD) filter [17] and the Gamma-Gaussian inverse Wishart probability hypothesis density (GGIW-PHD) filter to track multiple elliptical extension targets with this method. Unfortunately, these random matrix-based filters were only relevant in specific tracking circumstances where ellipsoids may approximate the target expansion well. Hence, the random hypersurface model (RHM) [18], [19] that assumes a diverse range of measurement sources from a scaled hypersurface with shape bounds was proposed as another target extension modeling strategy.

This model could notably track primary elliptical and sophisticated extended targets, such as star-convex shapes. For group target segmentation, the distance-based group target segmentation algorithm proposed by Granström et al. [20], [21] is a more extensively utilized method. Still, when the target shape size and the distance between targets are close, while this algorithm is less strategic for clustering, UAV cluster targets on infrared images offer small target groups, making statistical characteristics invisible. Therefore, clustering based on distance information that can only influence quantitative classification results is required.

According to the comprehensive reference review, three issues should be addressed for focal-plane UAV cluster target tracking:

1) The relatively limited research on UAV cluster target tracking currently, while only the motion characteristics of the UAV cluster target are considered when tracking the UAV cluster target, the infrared imaging characteristics of the UAV cluster target are not fully considered. The UAV cluster target tracking is also not realized on the focal plane.

2) Most current research on cluster target tracking employs the random matrix model for quantitative modeling, but this model does not account for the sensor's inherent noise and low estimation accuracy. Meanwhile, it cannot identify the splitting process of the target accurately.

3) The current δ-GLMB filter framework for measurement division primarily depends on distance division, but it does not meet the cluster tracking demands such as UAV clusters.

Accordingly, this paper proposes an algorithm for UAV cluster target tracking on the focal plane based on RHM-δ-GLMB, with the following significant contributions:

1) Initially, the RHM model is embedded in the δ-GLMB filter to estimate the motion and extended states of the UAV cluster target center of mass on the focal plane.

2) Next, we establish an elliptical RHM-based measurement model to map the measurement, state parameters, scaling factors, and errors to pseudo-measurement "0", then develop pseudo-measurement equations to reflect the target's extended shape size and resolve the problem that the random matrix model cannot realize target splitting and merging.

3) Finally, we implement the grid-based fast density-based spatial clustering of applications with noise (DBSCAN) measurement partitioning algorithm based on image element magnitude information in the measurement update to overcome the distance-based partitioning method constraints for infrared radiation (IR) measurement data partitioning.

The remainder of this paper is organized as follows: Section II introduces the RHM, Section III implements the proposed algorithm, Section IV illustrates the simulation data/analysis, and Section V summarizes the conclusion.

II. RANDOM HYPERSURFACE MODEL

This model efficiently estimates a target's extended state by integrating target shape parameters and motion state into the filtering algorithm.

A. ELLIPTIC RHM DEFINITION

Since the actual shape of the extended target is uncertain, an elliptical shape is commonly used to approximate the actual shape of the target. Another motivation for choosing an elliptic shape is that the ellipse's long axis can indicate the direction of the target's motion. Thus, an ellipse in the two-dimensional plane was defined as:

$$\left\{ z \mid z \in \mathbb{R}^2, (z - r_k)^T A_k^{-1} (z - r_k) \leq 1 \right\} \quad (1)$$

where r_k is the ellipse center position, A_k is the positive definite matrix used to describe the shape of the ellipse, including the long axis, short axis, and direction angle of the ellipse, and the positive definite matrix A_k is Cholesky decomposed to simplify the calculation [22]:

$$A_k = L_k L_k^T \quad (2)$$

$$L_k = \begin{bmatrix} l_k^{(1)} & 0 \\ l_k^{(3)} & l_k^{(2)} \end{bmatrix} \quad (3)$$

where, L_k is the lower triangular matrix of A_k's Cholesky decomposed, $l_k^{(1)}, l_k^{(2)}, l_k^{(3)}$ are the partitioned matrixes of L_k. Consequently, the target shape parameter at the moment k was obtained as $\varsigma_k = [l_k^{(1)}, l_k^{(2)}, l_k^{(3)}]^T$. Combining it with the state vector of the target, the target state at the moment k was obtained again, denoted as

$$x_k = [r_k, \varsigma_k]^T \quad (4)$$

The boundary shape equation of the new ellipse was also obtained:

$$g(z, \varsigma_k) = (z - r_k)^T \cdot \left(L_k L_k^T \right) \cdot (z - r_k) \quad (5)$$

Finally, by reducing the shape of the extended target according to a specific ratio s_k ($s_k \in [0, 1]$), we obtain the ellipse RHM. The boundary equation of the extended target is shown below:

$$\mathcal{O}(x_k) = \left\{ \begin{array}{l} z_k \mid z_k \in \mathbb{R}^2, g(z_k, x_k) \\ = (z_k - r_k) \left(L_k L_k^T \right)^{-1} (z_k - r_k)^T - 1 \end{array} \right\} \quad (6)$$

The reduced elliptic boundary equation is given by

$$\tilde{\mathcal{O}}(x_k) = \left\{ \begin{array}{l} z_k \mid z_k \in \mathbb{R}^2, g^*(z_k, x_k) \\ = (z_k - r_k) \left(L_k L_k^T \right)^{-1} (z_k - r_k)^T - s_k^2 \end{array} \right\} \quad (7)$$

B. ELLIPTICAL RHM-BASED MEASUREMENT MODEL

A target measurement can be represented by a measurement source y_k^l on an elliptical target surface and the additive noise v_k^l of the sensor itself. As shown in Fig. 1, the corresponding measurement equation for the elliptical target surface measurement source y_k^l is

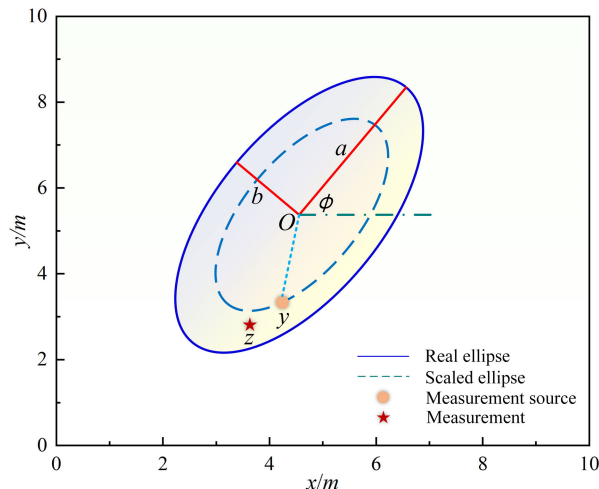$$z_k^l = y_k^l + v_k^l \quad l = 1, 2, \cdots, n \quad (8)$$

FIGURE 1. Schematic showing the elliptical RHM measurement model.

where the additive noise v_k^l of the sensor itself is Gaussian white noise with mean 0 and variance R_k. n denotes the number of measurements obeying the Poisson distribution.

Assuming that $\bar{S}$ is the extended target's boundary, the measurement source of the RHM model was described as

$$y_k^l \in r_k + s_k \cdot \mathcal{O}(x_k) \quad (9)$$

The elliptical RHM was then expressed as polar coordinates to facilitate the calculation.

$$y_k^l = r_k + s_k \cdot R\left(\theta_k^l; a_k, b_k, \varphi_k \right) \cdot e_k \quad (10)$$

$$R(\theta; a, b, \varphi) = \frac{ab}{\sqrt{[a\sin(\theta - \varphi)]^2 + [b\cos(\theta - \varphi)]^2}} \quad (11)$$

$$e_k = \begin{bmatrix} \cos\theta_k^l & \sin\theta_k^l \end{bmatrix}^T \quad (12)$$

where the centroid is $r_k = [r_{xk}, r_{yk}]^T$, a and b are the long and short axes of the ellipse, φ is the rotation angle of the ellipse, representing the angle between the long axis of the ellipse and the positive semi-axis of the x-axis, $\varphi \in [0, 2\pi]$; θ is the coordinate parameter; e_k is the unit vectors from polar to Cartesian coordinates [22].

Substituting (10) into (8), we obtained an equation for the ellipse RHM in terms of measurement.

$$\begin{aligned} z_k^l &= r_k + s_k \cdot R\left(\theta_k^l; a_k, b_k, \varphi_k \right) \cdot e_k + v_k^l \\ &= h(x_k, z_k, s_k) + v_k^l \end{aligned} \quad (13)$$

where θ_k^l is unknown, and the angle approximates the vector from the measurement point to the ellipse's center at the x-axis.

Finally, we introduce a pseudo-measurement equation to reduce the influence of θ_k^l on the extended target state estimation

$$h\left(x_k, z_k^l, s_k^l, v_k^l \right) = 0 \quad (14)$$

TABLE 1. The grid fast DBSCAN algorithm steps.

Algorithm Grid-Fast DBSCAN
Input: Measurement data set D, Radius parameter Cr; Minimal number of neighboring points *MinPts*
Output: Measurement division unit
Procedure:
Step 1:
Calculate the core point in D according to the given Cr and *MinPts* The core points obtained by the solution are then arranged in descending order according to density, then recorded as set S.
Step 2:
Select the point q with the highest density in set S every time, create a new class cluster M, and delete q from set S. For the point with a class label in the neighborhood of q, mark all points in D with the same class as M. Also, mark the class number of the remaining points in the e neighborhood of q as N, then delete the core points in the Cr neighborhood of q from the set S.
Step 3:
Cluster the remaining points in D to the class where the nearest core point in its neighborhood is located. Those without core points are marked as noise points.

The function $h(x_k, z_k^l, s_k^l, v_k^l)$ is calculated in APPENDIX. It maps the measurements, state parameters, scaling factors, and errors to pseudo-measurement "0", which is the essential difference between the measurement equations constructed by the elliptical RHM model and those created by other group target tracking algorithms.

III. ELLIPTIC RHM-BASED GAMMA-GAUSSIAN HYBRID δ-GENERALIZED LABEL MULTI-BERNOULLI FILTERING

A. GRID-FAST DBSCAN MEASUREMENT SEGMENTATION BASED ON IMAGE ELEMENT MAGNITUDE INFORMATION

This study applied a fast DBSCAN approach to rapidly distinguish between targets and noise points in sparse grids, avoiding DBSCAN's low clustering accuracy due to global parameter usages to reduce the algorithm's time complexity considerably.

While Table 1 presents the grid-fast DBSCAN algorithm's operation stages, Fig. 2 depicts the flowchart of the grid-fast DBSCAN measurement partitioning algorithm based on image element magnitude information.

We employed the DBSCAN measurement classification algorithm based on image element magnitude information. The algorithm clusters focal plane measurement data utilizing the grid-based clustering strategy, differentiates the dense grid from the sparse grid, links the neighboring dense grid into clusters, and labels the points in the sparse grid as noise points. Consequently, we observed many local maxima in the measurement set since the superposition of image element magnitudes at the clustering of UAV cluster targets on the focal plane generated a wave peak, and the development of a wave trough at a smaller number of UAV cluster targets formed a wave trough.

B. THE RHM-δ -GLMB ALGORITHM

1) BASIC CONCEPTS OF LABEL MULTI-BERNOULLI (LMB) FILTER

We used the regeneration probability r of a single target and the information that the target obeys the state space distribution $p(\cdot)$ to illustrate the uncertainty of a target's regeneration in Bernoulli RFS. The Bernoulli RFS probability density function was single, as shown below

$$\pi(X) = \begin{cases} 1 - r & X = \Phi \\ r \cdot p(X) & X = \{X\} \end{cases} \quad (15)$$

We also obtained the multi-Bernoulli RFS probability density function, as shown below:

$$\pi(\{x_1, x_2, \cdots, x_n\}) = \prod_{j=1}^{M}(1 - r^{(j)}) \times \sum_{1 \le i_1 \ne \cdots \ne i_n} \prod_{j=1}^{n} \frac{r^{(i_j)}p^{(i_j)}(x_j)}{1 - r^{(i_j)}} \quad (16)$$

The probability density was indicated as $\pi = \{(r^{(i)}, p^{(i)})\}_{i=1}^{M}$, and the cardinality distribution of the multi-Bernoulli RFS was presented as follows, disregarding the spatial distribution in (16) above.

$$\rho(n) = \prod_{j=1}^{M}(1 - r^{(j)}) \times \sum_{1 \le i_1 \ne \cdots \ne i_n} \prod_{j=1}^{n} \frac{r^{(i_j)}}{1 - r^{(i_j)}} \quad (17)$$

In a previous study, [13] extended the label to address the problem of disordered items in a set of target states *via* the conventional RFS theory-based multi-extended target tracking, $x \in X$.

Target states labeled RFS was exhibited as

$$X = \{(x, \ell)_i, i = 1, 2, \ldots, |X|\} \quad (18)$$

where x denotes the target state vector, $\ell \in \mathbb{L}$ is the label corresponding to the target, $\mathbb{L}$ denotes the label space, $|x|$ denotes the cardinality of the target state set, the label ℓ can be represented by $\ell = (k, i)$, k denotes the time when the target is newborn, and i indicates a different newborn target at the moment. Fig. 3 illustrates the target's label.

For the convenience of subsequent studies, several concepts are given as follows:

The multiobjective index of the real-valued function $h(\cdot)$ is defined as

$$[h(\cdot)]^x = \prod_{x \in x} h(x) \quad (19)$$

the generalized Kronecker δ function is defined as

$$\delta_Y(X) = \begin{cases} 1 & X = Y \\ 0 & X \ne Y \end{cases} \quad (20)$$

the inclusion function is defined as

$$1_Y(X) = \begin{cases} 1 & X \subseteq Y \\ 0 & otherwise \end{cases} \quad (21)$$
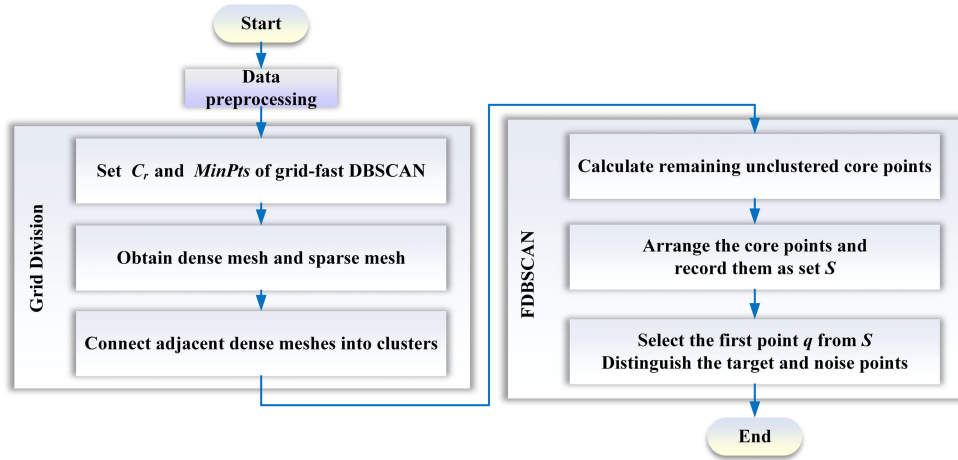
FIGURE 2. Algorithm flow chart showing the grid-fast DBSCAN measurement partitioning.
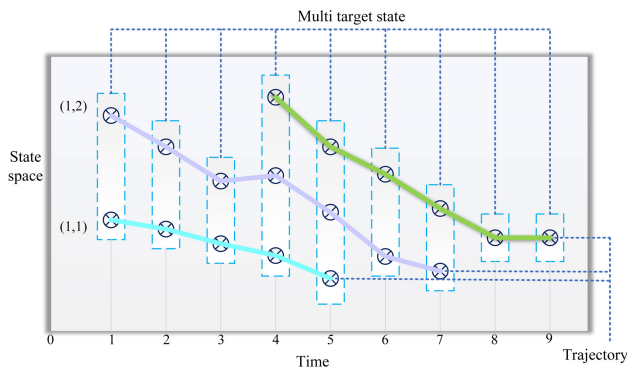

FIGURE 3. Schematic showing the target label.

the inner product of the functions $f(x)$ and $g(x)$ is defined as

$$\langle f, g \rangle \triangleq \int f(x)g(x)\mathrm{d}x \qquad (22)$$

The label set of RFS X can be represented on the target space $\mathbb{X} \times \mathbb{L}$ as $\mathcal{L}(X) = \{\mathcal{L}(x) : x \in X\}$, where $\mathcal{L} : \mathbb{X} \times \mathbb{L} \to \mathbb{L}$ is a map of $\mathcal{L}((x, \ell)) = \ell$. When the target state set X's cardinality equaled the label set's cardinality $\mathcal{L}(X) = \{\mathcal{L}(x) : x \in X\}$, X was distinctly labeled, and the function indicated discrete labels $\Delta(X) = \delta_{|X|}(|\mathcal{L}(X)|) = 1$.

Since the parameter set represents the labeled multi-Bernoulli RFS $\pi = \{(r^{(\zeta)}, p^{(\zeta)}), \zeta \in \Psi\}$, the probability density function of the labeled multi-Bernoulli RFS in the target space $\mathbb{X} \times \mathbb{L}$ can be described as

$$\pi\left(\{(r_1, \ell_1), \ldots, (r_n, \ell_n)\}\right)$$
$$= \delta_n\left(|\{\ell_1, \ldots, \ell_n\}|\right) \prod_{\zeta \in \Psi} \left(1 - r^{(\zeta)}\right)$$
$$\times \prod_{j=1}^{n} \frac{1_{\alpha(\Psi)}\left(\ell_j\right) r^{(\alpha^{-1}(\ell_j))} p^{(\alpha^{-1}(\ell_j))}\left(x_j\right)}{1 - r^{(\alpha^{-1}(\ell_j))}} \qquad (23)$$

For the convenience of subsequent studies, (23) was also abbreviated as $\pi = \{(r^{(\zeta)}, p^{(\zeta)})\}_{\zeta \in \Psi}$, and the LMB

probability density function corresponding to the parameter set $\pi = \{(r^{(\ell)}, p^{(\ell)})\}_{\ell \in \mathbb{L}}$ was expressed as

$$\pi(X) = \Delta(X)\omega(\mathcal{L}(X))p^X \qquad (24)$$

where

$$\omega(L) = \prod_{i \in L} (1 - r^{(i)}) \times \prod_{i \in L} \frac{1_L(\ell)r^{(\ell)}}{1 - r^{(\ell)}} \qquad (25)$$

$$p(x, \ell) = p^{(\ell)}(x) \qquad (26)$$

2) RHM-δ-GLMB FILTER

The δ-GLMB filter is a unique form of the GLMB filter with a special structure in the index space. The δ-GLMB filter was derived as follows.

$$\mathbb{C} = \mathcal{F}(\mathbb{L}) \times \Xi \qquad (27)$$

$$\omega^{(c)}(L) = \omega^{(I,\xi)}(L) = \omega^{(\ell,\xi)}\delta_I(L) \qquad (28)$$

$$p^{(c)} = p^{(I,\xi)} = p^{(\xi)} \qquad (29)$$

where Ξ is the discrete space, ξ belongs to Ξ, and I is the set of trajectory labels.

At the k moment, the probability density of δ-GLMB RFS was obtained as follows:

$$\pi(X) = \Delta(X) \sum_{(I,\xi) \in \mathcal{F}(\mathbb{L}) \times \xi} \omega^{(I,\xi)}\delta_I(L(X)) \left[p^{(\xi)}\right]^X \qquad (30)$$

Its cardinality distribution was as follows:

$$\rho(n) = \sum_{(I,\xi) \in \mathcal{F}(\mathbb{L}) \times \Xi} \sum_{L \in \mathcal{F}(\mathbb{L})} \omega^{(I,\xi)}\delta_I(L(X))$$
$$= \sum_{(I,\xi) \in \mathcal{F}(\mathbb{L}) \times \Xi} \omega^{(I,\xi)} \qquad (31)$$

Finally, we incorporated the RHM model $x_k = [\zeta_k^T, \varsigma_k^T]^T$ into the description of the target motion state for δ-GLMB filtering, denoting the target motion state vector as ζ_k^T and the target shape parameter as ς_k^T. This paper also implemented the algorithm in Gaussian mixture form, using the

Gauss distribution to approximate the target state distribution, which can be denoted as $\mathcal{N}(\boldsymbol{x}_k; r_k, \boldsymbol{P}_k)$. Furthermore, we used γ distribution to approximate the target volume measurement rate distribution, which could be characterized as $\mathcal{GAM}(\gamma_k; \alpha_k, \beta_k)$.

The spatial probability density function of the target was also defined as

$$
\begin{aligned}
p(\xi_k) &\triangleq p(\gamma_k \mid z_{1:k}) \cdot p(\boldsymbol{x}_k \mid z_{1:k}) \\
&= \mathcal{GAM}(\gamma_k; \alpha_k, \beta_k) \cdot \mathcal{N}(\boldsymbol{x}_k; r_k, \boldsymbol{P}_k) = \mathcal{GG}(\gamma_k; \boldsymbol{x}_k)
\end{aligned}
\tag{32}
$$

Then, we denoted the spatial probability density of the target $\varepsilon_k = \{(\alpha_k, \beta_k, r_k, \boldsymbol{P}_k)\}$ to facilitate the study.

1. Prediction steps:

Since the previous time's posterior probability density was considered to be LMB RFS, its parameter set may be compiled as $\{(r^{(\ell)}, p^{(\ell)})\}_{\ell \in \mathbb{L}}$. Assuming the multi-extended target model to be LMB RFS, the parameter set was designated as $\{(r_B^{(\ell)}, p_B^{(\ell)})\}_{\ell \in \mathbb{B}}$.

Consequently, while we derived the predictive density of the multi-expansion target as LMB RFS $\mathbb{L}_+ = \mathbb{B} \cup \mathbb{L}$, ($\mathbb{B} \cup \mathbb{L} = \Phi$), the parameter set was obtained as follows:

$$
\begin{aligned}
\pi_+ &= \left\{\left(r_{+,s}^{(\ell)}, p_{+,s}^{(\ell)}\right)\right\}_{\ell \in \mathbb{L}} \cup \left\{\left(r_B^{(\ell)}, p_B^{(\ell)}\right)\right\}_{\ell \in \mathbb{B}} \\
&= \left\{\left(r_+^{(\ell)}, p_+^{(\ell)}\right)\right\}_{\ell \in \mathbb{L}_+}
\end{aligned}
\tag{33}
$$

where

$$
r_{+,S}^{(\ell)} = \eta_S(\ell) r^{(\ell)}
\tag{34}
$$

$$
p_{+,s}^{(\ell)} = \frac{\langle p_s(\cdot, \ell) f(x \mid \cdot, \ell), p(\cdot, \ell)\rangle}{\eta_s(\ell)}
\tag{35}
$$

$$
\eta_s(\ell) = \langle p_s(\cdot, \ell), p(\cdot, \ell)\rangle
\tag{36}
$$

In the above equations, $p_s(\cdot, \ell)$ is the survival probability of the trajectory and $f(x \mid \cdot, \ell)$ is the Markov transfer probability of a single target.

Assuming that the parameter set of the posterior probability density of the extended target at the previous moment is $\tau_{k+1} = \{(\alpha_{k+1}, \beta_{k+1}, r_{k+1}, \boldsymbol{P}_{k+1})\}$, the probability density parameters of the prediction space can be obtained according to the γ distribution and Kalman filtering-related theory as

$$
\alpha_{k+1|k} = \frac{\alpha_k}{\mu}
\tag{37}
$$

$$
\beta_{k+1|k} = \frac{\beta_k}{\mu}
\tag{38}
$$

$$
r_{k+1|k} = \left(F_{k+1|k} \otimes I_d\right) r_k
\tag{39}
$$

$$
\boldsymbol{P}_{k+1|k} = F_{k+1|k} \boldsymbol{P}_{k|k} F_{k+1|k}^T + \boldsymbol{Q}_{k+1|k}
\tag{40}
$$

2. Update step.

Because the elliptic RHM-based measurement model is a high-dimensional nonlinear pseudo-measurement model, the target state must be estimated utilizing linearization. Although the EKF algorithm is the standard linearization method, it is insufficient for solving the elliptic RHM-based

measurement model since it includes the goal state, the scaling factor, and measurement noise. Furthermore, this algorithm does not need to calculate the measurement Jacobi matrix. It rather uses the UT transform to estimate the Gauss term parameters via Sigma sampling points while retaining the Kalman filtering procedure.

Based on the above considerations, the objective $\boldsymbol{x}_k$ was expanded into an augmented matrix $\boldsymbol{x}_{aug} = [\boldsymbol{x}_k^T, \boldsymbol{s}_k, \boldsymbol{v}_k^T]^T$, with random variables $\boldsymbol{s}_k \sim N(\mu_s, \sigma_s^2/4)$, where the corresponding means and variances are

$$
\boldsymbol{m}_{aug} = \left[\boldsymbol{m}_{k+1|k}^T, \mu_s, \boldsymbol{0}_2^T\right]^T
\tag{41}
$$

$$
\boldsymbol{P}_{aug} = diag\left[\boldsymbol{P}_{k+1|k}, \sigma_s^2, \boldsymbol{R}_k\right]
\tag{42}
$$

Consequently, the UT transform of the augmented matrix generates Sigma sampling points:

$$
\begin{cases}
\chi_0 = \boldsymbol{m}_{aug} \\
\chi_i = \boldsymbol{m}_{aug} + \sqrt{(n+\lambda)}\boldsymbol{P}_{aug} & i = 1, 2, \ldots, d \\
\chi_i = \boldsymbol{m}_{aug} - \sqrt{(n+\lambda)}\boldsymbol{P}_{aug} & i = d+1, \ldots, 2d
\end{cases}
\tag{43}
$$

The weights of each sampling point are as follows:

$$
\begin{cases}
\omega_0^{(m)} = \lambda/(\lambda + n) \\
\omega_i^{(c)} = \lambda/(\lambda + n) & +1 - \alpha^2 + \beta \\
\omega_i^{(m)} = 0.5/(\lambda + n), & i = 1, 2, \ldots, 2d
\end{cases}
\tag{44}
$$

where the parameters are taken as $\lambda = \alpha^2(n + \kappa) - n$, $\alpha = 0.01$, $\kappa = 0$, $\beta = 2$.

We then solved the pseudo-measurements using the Sigma sample point set and updated them to obtain the mean z'' of the pseudo-measurements, the covariance S_{nz} and the covariance $\boldsymbol{P}_{xz}$ of the augmentation matrix. The update process is as follows:

$$
\hat{z}_{nz} = \sum_{i=1}^n \omega_i^{(m)} z_i = \sum_{i=1}^n \omega_i^{(m)} \boldsymbol{h}(\chi_i)
\tag{45}
$$

$$
S_{nz} = \sum_{i=1}^n \omega_i^{(c)} \left(z_i - \hat{z}_{nz}\right) \left(z_i - \hat{z}_{nz}\right)^T
\tag{46}
$$

$$
\boldsymbol{P}_{xz} = \sum_{i=1}^n \omega_i^{(c)} \left(\chi_i - \boldsymbol{m}_k^{aug}\right) \left(z_i - \hat{z}_{nz}\right)^T
\tag{47}
$$

$$
\boldsymbol{m}_k^{aug} = \boldsymbol{m}_k^{aug} + \boldsymbol{P}_{xz} \left(S_{nz}\right)^{-1} \left(0 - \hat{z}_{nz}\right)
\tag{48}
$$

$$
\boldsymbol{C}_k^a = \boldsymbol{C}_k^a - \boldsymbol{P}_{xz} \left(S_{nz}\right)^{-1} S_{nz} \left(\boldsymbol{P}_{xz} \left(S_{nz}\right)^{-1}\right)^T
\tag{49}
$$

Finally, we can obtain the updated set of parameters $\tau_{k+1} = \{(\alpha_{k+1}, \beta_{k+1}, r_{k+1}, P_{k+1})\}$ from the above equation, where

$$
\boldsymbol{m}_{k+1}^{(j),W} = \boldsymbol{m}_k^{aug}(1:n)
\tag{50}
$$

$$
\boldsymbol{P}_{k+1}^{(j),W} = \boldsymbol{C}_k^a(1:n)
\tag{51}
$$

$$
\alpha_{k+1}^{(j),W} = \alpha_{k+1|k}^{(j)} + |W|
\tag{52}
$$

$$
\beta_{k+1}^{(j),W} = \beta_{k+1|k}^{(j)} + 1
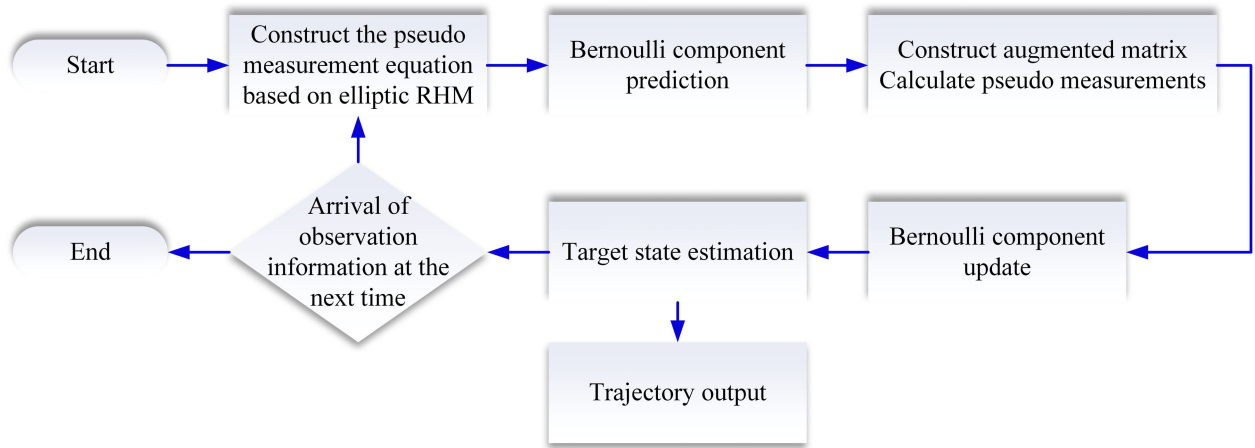\tag{53}
$$

FIGURE 4. Algorithm flow chart of the GGM-RHM-δ-GLMB.

The quantitative likelihood of the clustered set W is.

$$L_k^{(j),W} = \prod_{z \in W} \mathcal{N}(0; \hat{z}_{nz}) \tag{54}$$

$$L_k^{(j),\gamma} = \frac{1}{|W|!} \frac{\Gamma\left(\alpha_{k|k}^{(j),W}\right) \beta_{k|k-1}^{\alpha_{k|k-1}^{(j)}}}{\Gamma\left(\alpha_{k|k-1}^{(j)}\right) \left(\beta_{k|k}^{(j),W}\right)^{\alpha_{k|k}^{(j),W}}} \tag{55}$$

The updated LMB RFS can also be expressed as $\pi(\cdot \mid z) = \{(r^{(\ell)}, p^{(\ell)}(\cdot))\}_{\ell \in \mathbb{L}_+}$, where

$$r^{(\ell)} = \sum_{\substack{(I_+,\theta) \in \mathcal{F}(\mathbb{L}_+)}} \sum_{i=1}^{|I_k|+1} \sum_{\substack{u(\mathbf{Z}_k) \in P_i(\mathbf{Z}_k) \\ \theta \in \Theta(u(\mathbf{Z}_k))}} w_{u(\mathbf{Z}_k)}^{(I_k,\theta)} (I_k) 1_{I_k}(\ell) \tag{56}$$

$$p^{(\ell)}(\mathbf{x}) = \sum_{\substack{(I_+,\theta) \in \mathcal{F}(\mathbb{L}_+)}} \sum_{i=1}^{|I_k|+1} \sum_{\substack{u(z_k) \in P_i(z_k) \\ \theta \in \Theta(u(z_k))}} w_{u(z_k)}^{(I_k,\theta)}$$

$$\times (I_k) 1_{I_k}(\ell) p^{(I_k,\theta)}(\mathbf{x}, \ell) \tag{57}$$

$$p^{(I_k,\theta)}(\mathbf{x}_k, \ell \mid u(z_k))$$

$$= \frac{p^{(I_k,\theta)}(\mathbf{x}_k, \ell) \psi_{u(z_k)}(\mathbf{x}_k, \ell; \theta)}{\eta_{u(z_k)}^{(I_k,\theta)}(\ell)} \tag{58}$$

$$\eta_{u(z_k)}^{(I_k,\theta)}(\ell) = \langle p(\cdot, \ell), \psi_{u(z_k)}(\cdot, \ell; \theta) \rangle \tag{59}$$

$$\psi_{u(z_k)}(\mathbf{x}, \ell; \theta)$$

$$= \begin{cases} \dfrac{p_D(\mathbf{x}, \ell) g\left(u_{\theta(\ell)}(z_k) \mid \mathbf{x}, \ell\right)}{[\kappa(\cdot)]^{u_{\theta(\ell)}(z_k)}} & \theta(\ell) > 0 \\ 1 - p_D(\mathbf{x}, \ell) & \theta(\ell) = 0 \end{cases} \tag{60}$$

$$g(\bullet \mid \mathbf{x}, \ell) = L_k^{(j),W} L_k^{(j),\gamma} \tag{61}$$

where $p_D(\mathbf{x}, \ell)$ is the detection probability of the trajectory, $\kappa(\bullet)$ is the clutter density obeying the Poisson distribution, and Θ_{I_+} is the mapping from the measurement space to the state space: $I_+ \rightarrow \{0, 1, \cdots, |Z|\}$. The mapping is notably independent and non-repetitive.

3) ALGORITHM FLOW
Fig. 4 depicts the flow chart of the GGM-RHM-δ-GLMB algorithm. Table 2 displays the detailed implementation steps of the algorithm.

IV. SIMULATION
A. EVALUATION METRICS
This paper used the Optimal Sub-Pattern Assignment (OSPA) to evaluate the algorithm's performance. It can also more comprehensively determine the distance relationship between the estimated and real target sets: the smaller the OSPA, the better the algorithm can track the target.

First, we define the OSPA distance between two non-empty finite sets $X = \{x_1, x_2, \ldots, x_m\}$ and $Y = \{y_1, y_2, \ldots, y_m\}$ as [21], (62), as shown at the bottom of the page, where m and n are the cardinalities of the finite sets X and Y, respectively, c and p are the truncation and order parameters, respectively,

$$\bar{d}_p^{(c)}(X, Y) = \begin{cases} 0 & m = n = 0 \\ \left(\dfrac{1}{n}\left(\min_{\pi \in \Pi_n} \sum_{i=1}^{n} d^{(c)}(x_i, y_{\pi(i)})^p + c^p(n - m)\right)\right)^{1/p} & m \leq n \\ \bar{d}_p^{(c)}(Y, X) & m > n \end{cases} \tag{62}$$

with smaller c indicating smaller penalties for estimating errors in the number of targets and p generally taken as 2, and the distance between the state x and y is denoted as $d^{(C)}(x, y) = \min(c, d(x, y))$.

B. ANALYSIS OF THE EFFECT OF DIFFERENT MEASUREMEN DIVISION METHODS

Based on image element magnitude information, we subsequently compared the distance-based measurement technique with this paper's algorithm to validate further the efficiency of the proposed fast DBSCAN measurement division. The threshold value of the distance-based measurement was 3 pixels.

Furthermore, based on the UAV cluster simulation image infrared sequence, the simulation involved measurements at 50 s, 100 s, and 150 s. While the image size of the UAV cluster simulation image infrared sequence was 256×256 pixels, there were 25 UAVs altogether that could be split into six UAV subgroups throughout the flight.

Fig. 5 is on the previous page. Fig. 5(a)–(c) exhibit the UAV cluster simulation IR image sequences, Fig. 5(d)–(f) demonstrate the measurement division results based on distance division, and the three images in Fig. 5(g)–(i) show the measurement division results based on the grid-fast DBSCAN algorithm. The red point in the figure is the mass center of the UAV cluster after clustering, the yellow × is the real position of the UAV, and the blue ellipse is the extent of the UAV cluster target measurement.

Fig. 5 also depicts the algorithm's efficacy on focus plane quantitative segmentation. The reason for the poor quantitative segmentation results in Fig. 5(d)–(f) is dictated by the threshold value in the distance-based segmentation algorithm. As for the threshold, its value is too high to cause difficulty in capturing the UAV cluster clustering process, making the threshold value too low to produce a significant number of inaccurate clusters and causing redundant clusters for the infrared images of UAV clusters, where the targets are close to each other. Consequently, relying solely on the division of threshold values to achieve clustering for the UAV cluster target on the infrared image plane cannot fulfill the target tracking command.

This paper's proposed algorithm thus fully exploits the magnitude of the image elements in the UAV cluster infrared image sequences. It also determines the position of most targets during the initial clustering of the image plane measurement data via the grid-based clustering algorithm and clusters using the fast DBSCAN algorithm to achieve the UAV cluster targets. The experimental results demonstrate the algorithm's capabilities in the infrared scenario, providing reliable information for future UAV cluster target tracking.

C. PARAMETER SETTINGS

Given that the tracking time for the UAV cluster target is 150 s, the sampling time is 1 s, and the six UAV subgroups are all moving at a uniform speed in a straight line. Fig. 6 describes the motion trajectories of the six UAV cluster

TABLE 2. The GGM-RHM-δ-GLMB algorithm Implementation Steps.

Algorithm GGM-RHM-δ-GLMB
Input: The GGM component parameters, target regeneration probability $r_k^{(1)}$, and Measurement sets $\mathbf{Z}$
Output: Track trajectory
Procedure:
Step 1: Initialize the state
(1) Initialize the target newborn model
(2) Initialize the target label set
(3) Initialize the measurement set
Step 2: Construct the pseudo measurement equation
(1) Model the target measurement source using the RHM model
(2) Construct the pseudo measurement equation $h(\mathsf{g})$
Step 3: Predict
(1) Inherit the last surviving target label
(2) Predict the target regeneration probability $r_{k+1\|k}^{(1)}$
(3) Predict the state parameter set $\tau_{k+1\|k} = \left\{ \left(\alpha_{k+1\|k}, \beta_{k+1\|k}, r_{k+1\|k}, P_{k+1\|k} \right) \right\}$
(4) Predict the weight w of each GGM component and the weight $w^{(I_k, \theta)}(L)$
(5) Merge survival with the newborn target sets and merge labels
Step 4: Update
(1) Construct the state augmented matrix, solve the Sigma points, obtain the pseudo-measured values
(2) Transform LMB into δ-GLMB
(3) Update the state parameter set $\tau_{k+1} = \left\{ \left(\alpha_{k+1}, \beta_{k+1}, r_{k+1}, P_{k+1} \right) \right\}$
(4) Calculate the measurement likelihood function, update the weight w for each GGM component and the weight $\omega_{u(Z)}^{(I_k, \theta)}(L)$
(5) Transform δ-GLMB into LMB, obtain $r_{k+1}^{(1)}$ and $p_{k+1}^{(1)}$
Step 5: Estimate the target state
(1) Trim and merge the Gamma-Gaussian mixture components
(2) Judge whether $\left\{ r_k^{(1)} \right\}_1$ is greater than the threshold value.
(3) If the target $\left\{ r_k^{(1)} \right\}_1$ exceeds the threshold value, extract the target.
(4) However, if $k=k+1$, go back to Step 2
(5) Else, end the target tracking procedure

subgroups. Table 3 shows the simulated set parameters related to the centroid of the UAV cluster on the next page.

The target detection probability was 0.99, and the target survival probability was 0.98, with the clutter obeying a Poisson distribution with mean $\lambda = 15$ in the image plane, the scaling factor $s_k \sim \mathcal{N}(0.6, 0.07)$ in the RHM model, the gamma distribution parameter $\alpha = 10$, $\beta = 2$, and the target state, expressed as $\boldsymbol{x} = [x, y, v_x, v_y, a, b, \varphi]^T$. Consequently, state transfer and process noise matrixes were obtained as follows:

$$\boldsymbol{F} = \begin{bmatrix} 1 & 0 & 1 & 0 & 0 & 0 & 0 \\ 0 & 1 & 0 & 1 & 0 & 0 & 0 \\ 0 & 0 & 1 & 0 & 0 & 0 & 0 \\ 0 & 0 & 0 & 1 & 0 & 0 & 0 \\ 0 & 0 & 0 & 0 & 1 & 0 & 0 \\ 0 & 0 & 0 & 0 & 0 & 1 & 0 \\ 0 & 0 & 0 & 0 & 0 & 0 & 1 \end{bmatrix},$$
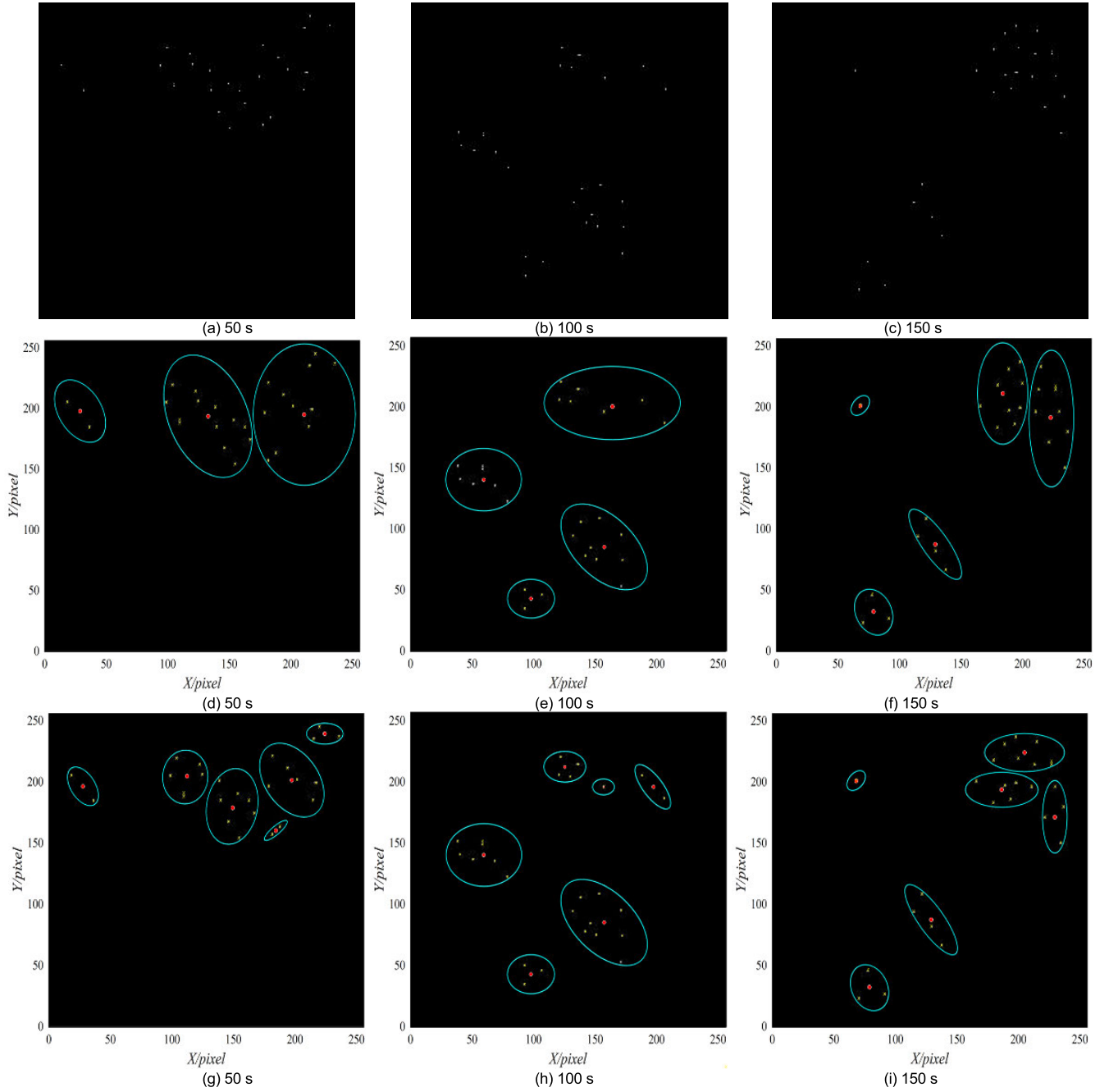
FIGURE 5. Clustering effects of different measurement division methods: (a)–(c) the UAV cluster simulation IR image sequences; (d)–(f) results based on distance division; (g)–(i) results based on the grid-fast DBSCAN.

$$Q = \begin{bmatrix} 0.01 & 0 & 0 & 0 & 0 & 0 & 0 \\ 0 & 0.01 & 0 & 0 & 0 & 0 & 0 \\ 0 & 0 & 4 & 0 & 0 & 0 & 0 \\ 0 & 0 & 0 & 4 & 0 & 0 & 0 \\ 0 & 0 & 0 & 0 & 1 & 0 & 0 \\ 0 & 0 & 0 & 0 & 0 & 1 & 0 \\ 0 & 0 & 0 & 0 & 0 & 0 & 1 \end{bmatrix} \quad (63)$$

Additionally, the target regeneration model was δ-GLMB RFS with distribution [23], [24]

$$\pi_\Gamma = \{(r_\Gamma^{(i)}, p_\Gamma^{(i)}), \ell_\Gamma^{(i)}\}_{i=1}^6 \quad (64)$$

where

$$r_\Gamma^{(1)} = r_\Gamma^{(2)} = 0.02 \quad (65)$$

$$r_\Gamma^{(3)} = r_\Gamma^{(4)} = r_\Gamma^{(5)} = r_\Gamma^{(6)} = 0.03 \quad (66)$$

$$p_\Gamma^{(i)}(x) = \mathcal{N}\left(x; m_\gamma^{(i)}, P_\gamma\right) \quad (67)$$

$$P_\gamma = diag([5\ 5\ 5\ 5]) \quad (68)$$

Table 4 displays the target distribution values on the top of the page.

TABLE 3. Parameter settings related to the centroid of the UAV cluster.

Time	Cluster number	Centroid Position/ pixel	Centroid Velocity/ pixel/s	Moments of appearance/s	Moments of disappearance/s
0–50 s	1	(125,200)	(−1, −2)	1	80
	2	(120,210)	(−1, −1)	20	101
	3	(160,180)	(−2, −2)	30	101
	4	(190,160)	(−1, −2)	40	101
	5	(205,195)	(−2, −2)	50	101
	6	(225,225)	(−2, −2)	70	101
50–100 s	1	(90,165)	(−1, −1)	1	80
	2	(115,105)	(−1, −1)	20	101
	3	(160,80)	(−1, −1)	30	101
	4	(145,215)	(−1, −2)	40	101
	5	(175,200)	(−2, −2)	50	101
	6	(205,195)	(−2, −2)	70	101
100–150 s	1	(85,25)	(−1, 1)	1	80
	2	(75,200)	(1, −1)	20	101
	3	(135,85)	(−1, −1)	30	101
	4	(185,195)	(−1, −2)	40	101
	5	(200,225)	(−2, −2)	50	101
	6	(225,175)	(−2, −2)	70	101

TABLE 4. The target distribution values.

	0-50 s	50-100 s	100-150 s
$m_\gamma^{(1)}$	[125 -1 200 -2]	[90 -1 165 -1]	[85 -1 25 -1]
$m_\gamma^{(2)}$	[120 -1 210 -1]	[115 -1 105 -1]	[75 -1 200 -1]
$m_\gamma^{(3)}$	[160 -2 180 -2]	[160 -1 80 -1]	[135 -1 85 -1]
$m_\gamma^{(4)}$	[190 -1 160 -2]	[175 -2 200 -2]	[185 -1 195 -2]
$m_\gamma^{(5)}$	[205 -2 195 -2]	[205 -2 195 -2]	[200 -2 225 -2]
$m_\gamma^{(6)}$	[225 -2 225 -2]	[145 -1 215 -2]	[225 -2 175 -2]

TABLE 5. Statistical OSPA distance characteristics for the 0-150 s IR image sequences.

Time	Algorithm	OSPA Distance		OSPA Location		OSPA Cardinality	
		Mean	Range	Mean	Range	Mean	Range
0─50 s	GMM-ET-PHD	3.500	[0.820,13.685]	3.165	[0.820, 6.775]	0.667	[0, 12.5]
	GMM-RHM-PHD	3.463	[1.213,16.210]	2.796	[0.746, 5.741]	0.458	[0, 12.5]
	GGM-RHM-δ-GLMB	2.774	[1.040,13.776]	2.315	[1.041, 5.023]	0.333	[0,4.167]
50─100 s	GMM-ET-PHD	5.934	[0.833,11.835]	5.276	[0.833,11.835]	0.658	[0, 5]
	GMM-RHM-PHD	2.888	[0.531, 6.880]	2.721	[0.531, 6.350]	0.417	[0,8.333]
	GGM-RHM-δ-GLMB	2.721	[0.618,10.368]	2.304	[0.618, 6.012]	0.167	[0,4.167]
100─150 s	GMM-ET-PHD	5.756	[0.620,16.021]	4.238	[0.349,12.424]	1.517	[0, 12.5]
	GMM-RHM-PHD	3.409	[1.213,16.210]	2.867	[0.746, 7.775]	0.542	[0, 12.5]
	GGM-RHM-δ-GLMB	2.400	[0.705, 6.192]	2.273	[0.705, 4.369]	0.125	[0,4.167]

### D. ANALYSIS OF THE EFFECT UNDER DIFFERENT TRACKING ALGORITHMS FOR UAV CLUSTER TARGET TRACKING

We chose the GGM-RHM-PHD [25] and GMM-ET-PHD [26] algorithms to validate the effectiveness of the GGM-RHM-δ-GLMB algorithm developed in the UAV cluster target tracking. On the next page, Fig. 7 presents the simulation results, including the infrared pictures. The figure's comparative effects of the GMM-ET-PHD and GMM-RHM-PHD algorithms represent the obvious advantages of integrating the RHM model to establish the measurement model. Although the centroid positions of the UAV subclusters estimated by both algorithms were close to the center of

the pixel clusters on the real focal-plane UAV subclusters, some discrepancies existed between the estimation results of the two figures. We also observed that the GMM-RHM-PHD and GGM-RHM-δ-GLMB algorithms depicted in this paper more accurately characterized the UAV cluster target state. The fundamental cause of this occurrence is the improved precision of the measurement model developed using the RHM model.
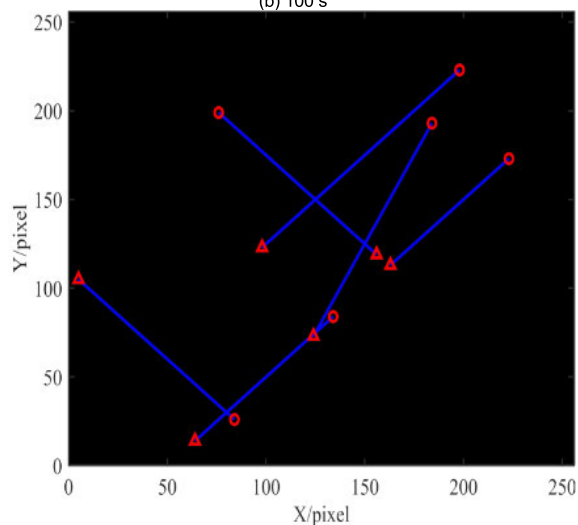
Simultaneously, the performance of this paper's algorithm exceeded the GMM-RHM-PHD algorithm, primarily because the GMM-RHM-PHD algorithm used a random matrix model in the measurement division process and the method of updating the target motion state stimulated the
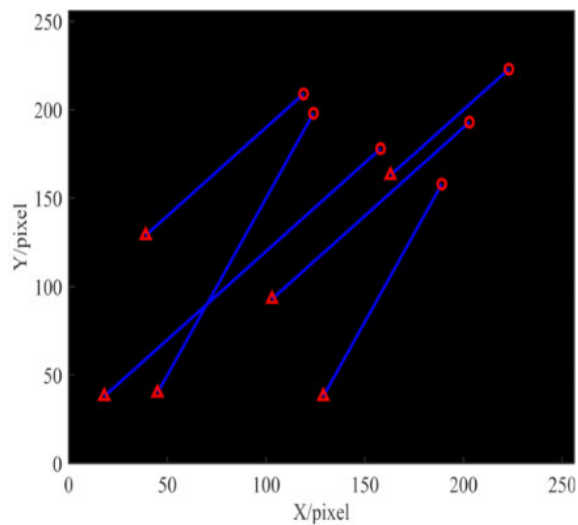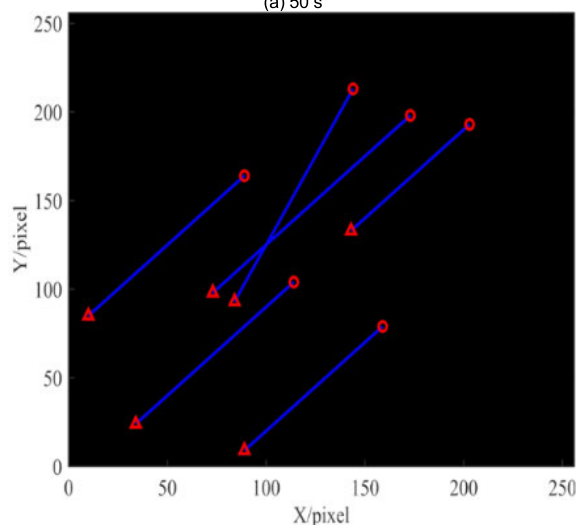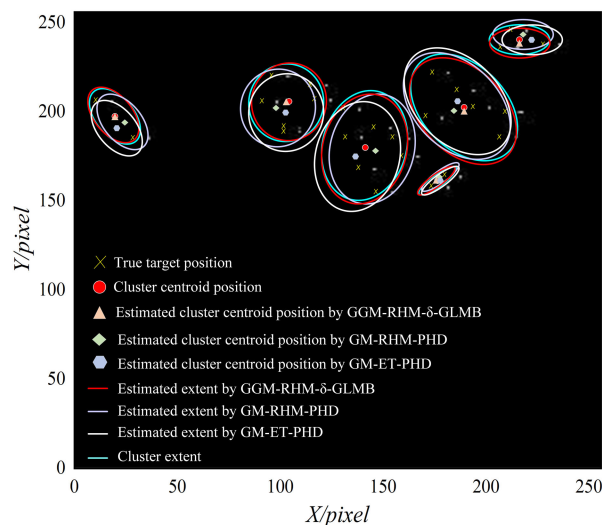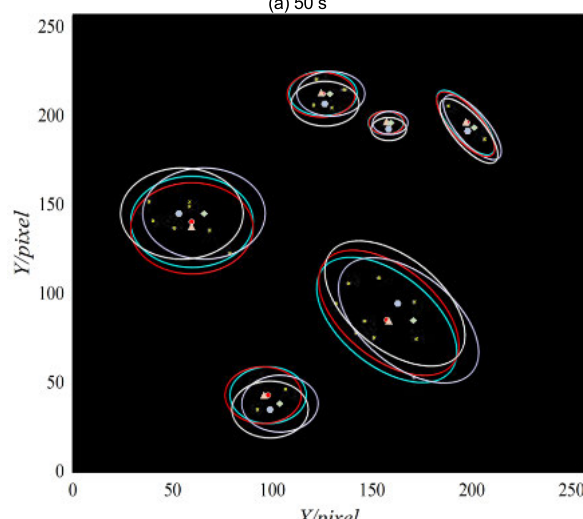
FIGURE 6. UAV cluster motion trajectory at 50 s, 100 s and 150 s.

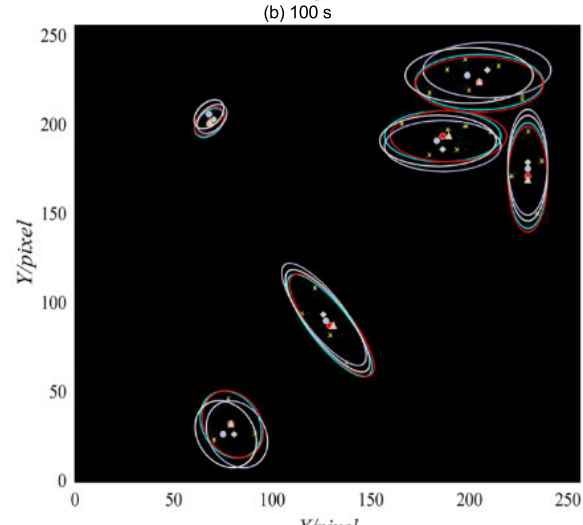**FIGURE 7.** Tracking results under different algorithms at 50 s, 100 s and 150 s.

accumulation of measurement errors, affecting the estimation of the UAV cluster target state. Since the suggested algorithm

used the UKF algorithm instead to solve the measurement Jacobi matrix, the Gauss term parameters were calculated

utilizing the Sigma sampling points, preserving the Kalman filtering process and enhancing the algorithm's target state estimation performance.

Afterward, we assessed the three algorithms via 100 Monte Carlo Simulations to evaluate their performance further. On page 11–12, Figs. 8–10 display the target tracking results of the three algorithms for the simulated UAV cluster IR image sequences within 0–150 s. We observed from the figures that although the three systems could track six UAV subgroups, disparities existed in their tracking effects, with this paper's algorithm providing an excellent tracking performance. Furthermore, while the tracking trajectory had far more overlap with the real trajectory, it had the least overlap with the fake trajectory. In contrast, the trajectory overlap of the other two algorithms diminished compared to this paper's algorithm, mainly because the GMM-ET-PHD algorithm had more spurious trajectories in the tracking process and, thus, a poor tracking effect.

On page 14. Fig. 11 illustrates the OSPA curves of the three algorithms within 0–150 s, Fig. 12 highlights the tracking cardinality estimation curves of the three algorithms within 0–150 s, and Table 5 displays the related OSPA distance statistical properties in 0–150 s. Fig. 11 verified the tracking effectiveness of the three algorithms in Figs.8–10 and depicted the performance of this paper's algorithm for UAV cluster target tracking. Interestingly, the OSPA distance fluctuation in this paper's algorithm was lower than in the other two algorithms because the proposed algorithm exploited RHM for measurement modeling after applying the fast grid DBSCAN algorithm for measurement division. It also added a corresponding label to the target state, thus avoiding error accumulations in the estimation process.

Although the GMM-RHM-PHD algorithm employed the RHM model for quantitative modeling, its PHD filtering algorithm only obtained the target's probability density at this moment in tracking the extended target rather than forming a continuous tracking trajectory of the target. In this paper, the δ-GLMB algorithm in the framework of the LMB algorithm could thus properly estimate the goal state and provide a continuous tracking trajectory with minimal tracking error. Even though the GMM-ET-PHD algorithm could track extended targets, improving the target measurement division and self-adaptability in the GMM-ET-PHD algorithm, which has high operational complexity and less accurate estimation of the number of targets when compared with the algorithm in this paper and the GMM-RHM-PHD algorithm, was still needed. Meanwhile, when coupled with the statistical OSPA distance characteristics of the three different algorithms illustrated in Table 5, the adaptability and stability of this paper's suggested method were compared to other algorithms.

Fig. 12 suggests that although the two compared algorithms largely deviated from the target estimations, causing significantly larger fluctuations in the GMM-ET-PHD algorithm within 0–10 s, all three algorithms fluctuated within 70–85 s, making this paper's algorithm experience the smallest fluctuation range. When estimating the measurement of
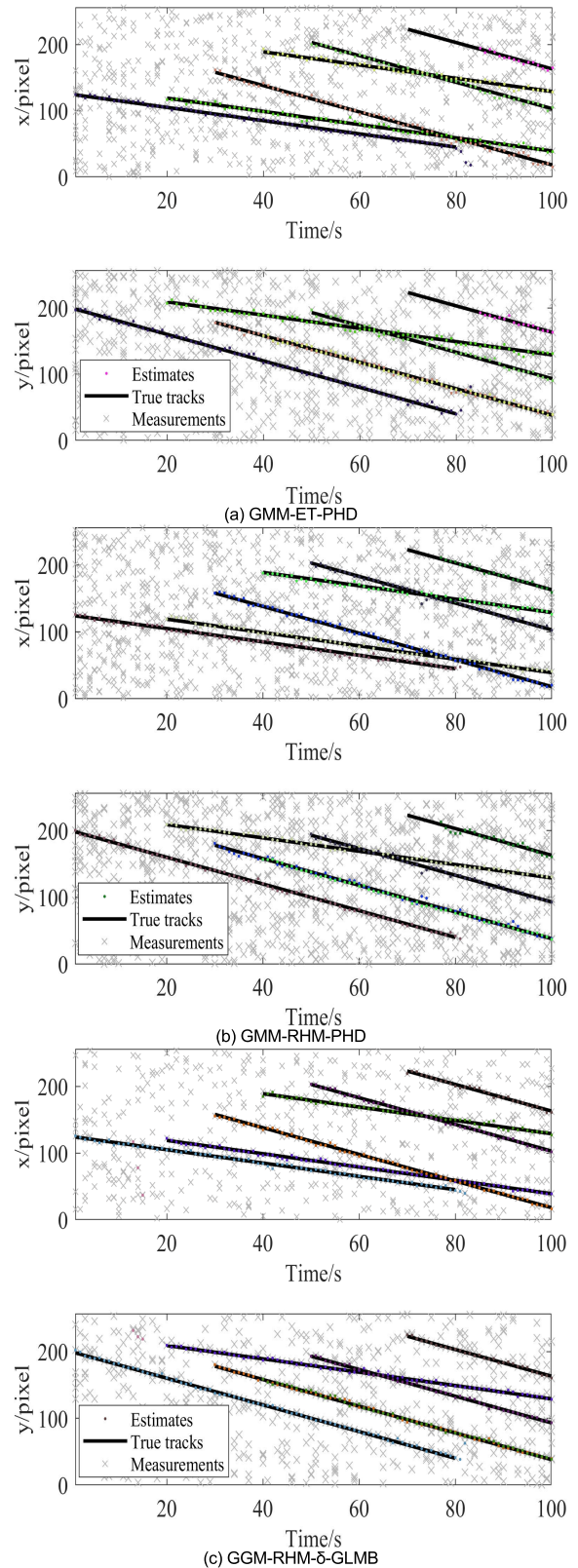

FIGURE 8. Effects of the three algorithms on UAV cluster target tracking within 0–50 s.

other targets in the region of the nascent target, an error generally triggers a bias in estimating the state of the target. Since
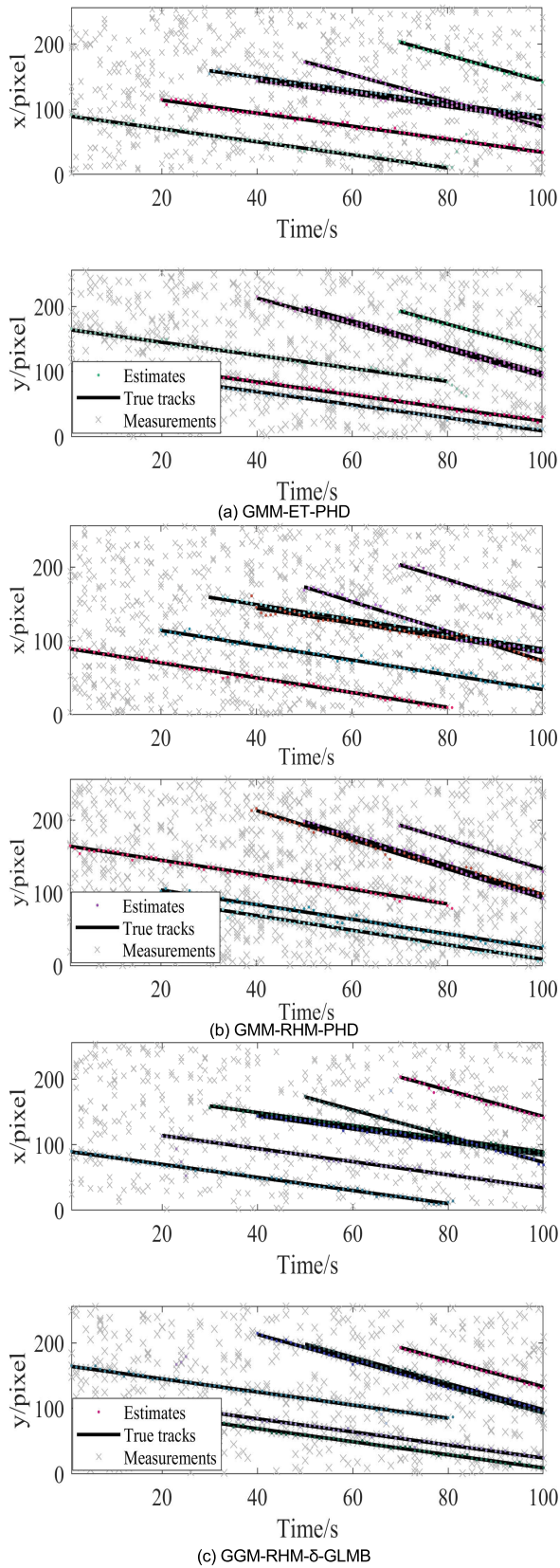
FIGURE 9. Effects of the three algorithms on UAV cluster target tracking within 50–100 s.
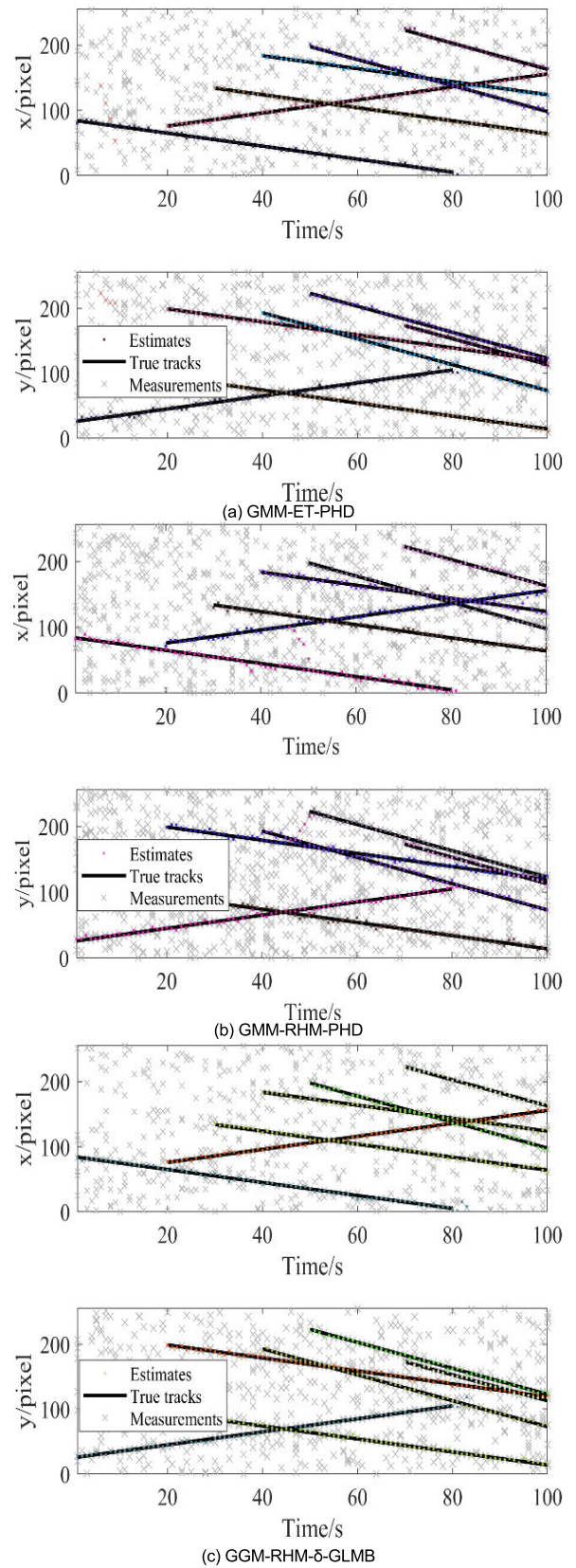

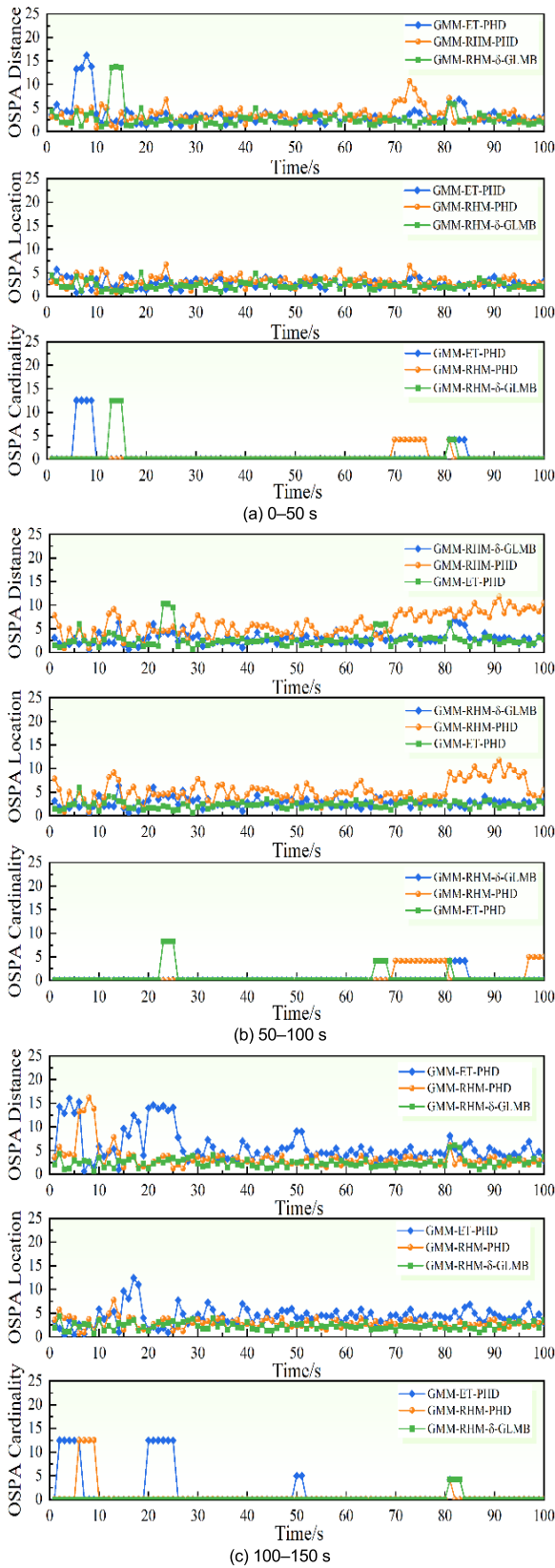**FIGURE 10.** Effects of the three algorithms on UAV cluster target tracking within 100–150 s.

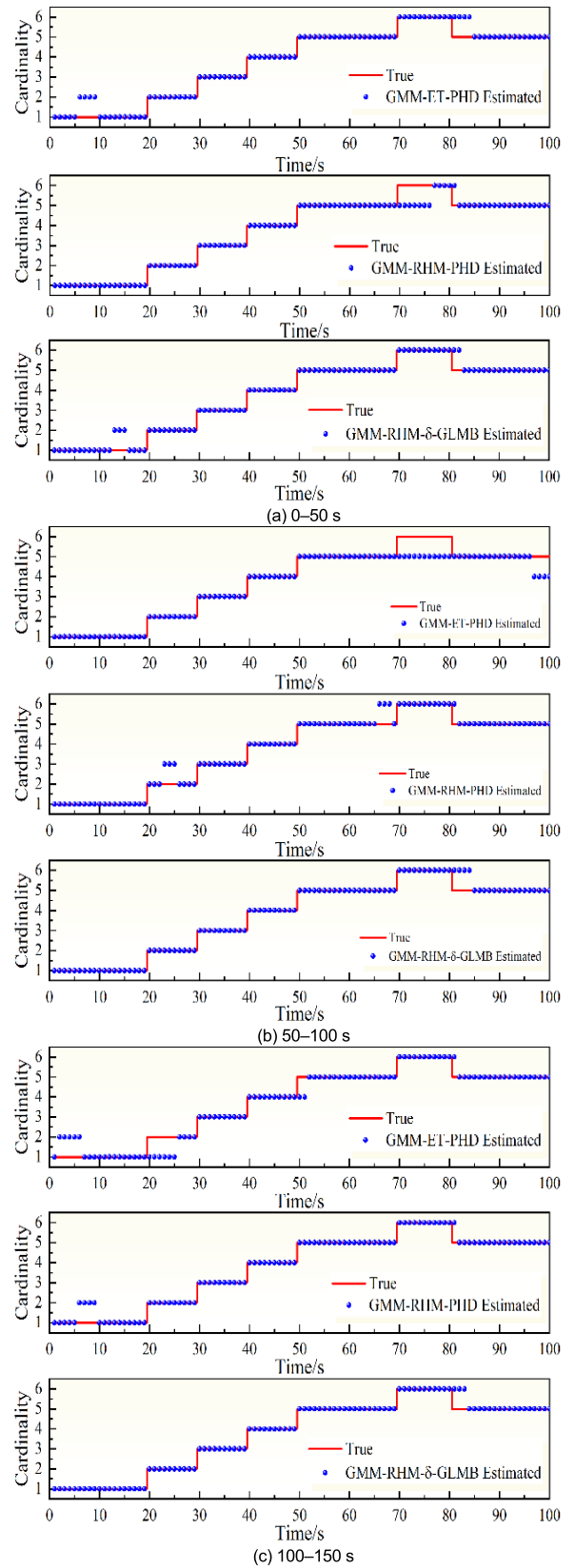**FIGURE 11.** The three algorithms' OSPA curves within 0–50 s, 50—100 s, 100-150 s.

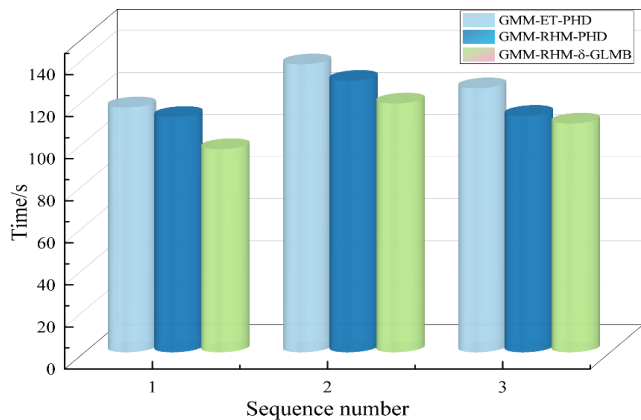**FIGURE 12.** The three algorithms for tracking cardinality estimation 0–50 s, 50—100 s, 100-150 s.

FIGURE 13. Running time of the three algorithms.

the clutter can be spread in the neighborhood of the newborn target, the algorithm mistakenly perceives it as a target. It then incorrectly distributes the weight of the Bernoulli component, resulting in a bad final tracking effect.

The running time comparison curves of the three algorithms are given in Fig. 13 on page 15. Fig. 13 reveals that this paper's algorithm had a minimum running time. The three algorithms' design processes were mostly responsible for this scenario. Therefore, the algorithm proposed in this paper was optimized throughout the design phase via the δ-GLMB algorithm, providing highly parallel processing performances by introducing the label space. Notably, it did not increase the algorithm's running duration since the GMM-ET-PHD algorithm solved the probability density of the target and performed data association to maintain the tracking trajectory's continuity.

V. CONCLUSION

This paper proposes an RHM-δ-GLMB-based algorithm for UAV cluster tracking on the focal plane that embeds the RHM model into the δ-GLMB filter, for the case of a single transmitter and two receivers, specifies the degree of target expansion with the RHM model, fully utilizes the merits of the δ-GLMB filter in handling extended multi-target tracking, and ultimately implements the proposed algorithm in the form of the Gamma-Gaussian mixture to increase the accuracy of the algorithm,. Since this paper's simulation results demonstrate that the model and algorithm had certain improvements over the previous models and algorithms, some conclusions could be drawn. First, the simulation compared the algorithm of this research with distance-based measurement division. This paper's algorithm could employ the imaging characteristics of the focal plane to eliminate false and redundant clustering triggered by selecting the threshold value in the distance-based division algorithm, demonstrating the advantages of the outlook in the infrared scenario. Therefore, we simulated and analyzed the simulation results of the three tracking algorithms on the IR image sequences of the UAV cluster targets within 0–150 s in a single simulation.

According to the focal plane tracking results, this algorithm consistently tracked UAV clusters on the focal plane, however, the other two algorithms had considerable discrepancies in UAV cluster centroid position and shape estimation. Finally, we used 100 Monte Carlo experiments to prove the effectiveness of this paper's algorithm for UAV cluster IR image sequences, after which the advantages of this paper's algorithm in the target centroid motion and extended states were demonstrated by comparing the OSPA distance, cardinality estimation, and running time of this paper's algorithm to the GMM-RHM-PHD and GMM-ET-PHD algorithms.

In practical scenarios, a UAV cluster's movement may take on various complicated motions, including splitting and merging. In the following study, we will consider the impact of the complex movement of the UAV cluster on the effect of the tracking algorithm. Additionally, when the quantity of UAVs rises and the density of the cluster increases, whether the algorithm can achieve stable tracking of the target is also the focus of subsequent research. Meanwhile, we anticipate that the algorithm will be validated for more complicated scenarios and the real measured data in future work.

APPENDIX

Based on Sections II-A and II-B, the equation of the ellipse where any measurement source is located in

$$(z - r_k)^T \mathbf{A}_k^{-1} (z - r_k) - s_k^2 = 0 \qquad (A1)$$

Let

$$g\left(\boldsymbol{x}_k, z_k^l, s_k^l\right) \triangleq \left(z_k^l - r_k\right)^T \mathbf{A}_k^{-1} \left(z_k^l - r_k\right) - s_k^l \qquad (A2)$$

Substituting (1) in this equation yields

$$g\left(\boldsymbol{x}_k, z_k^l, s_k^l\right)$$
$$= g(\boldsymbol{x}_k, \boldsymbol{y}_k^l + \boldsymbol{v}_k^l, s_k^l)$$
$$= \underbrace{g(\boldsymbol{x}_k, \boldsymbol{y}_k^l, s_k^l)}_{=0} + 2\left(\boldsymbol{y}_k^l - r_k\right)^T \mathbf{A}_k^{-1} \boldsymbol{v}_k^l + \boldsymbol{v}_k^l \mathbf{A}_k^{-1} \boldsymbol{v}_k^l$$

$$(A3)$$

Then, by separating the non-zero and zero-containing terms, we can obtain that

$$0 = g\left(\boldsymbol{x}_k, z_k^l, s_k^l\right) - 2\left(\boldsymbol{y}_k^l - r_k\right)^T \mathbf{A}_k^{-1} \boldsymbol{v}_k^l - \boldsymbol{v}_k^l \mathbf{A}_k^{-1} \boldsymbol{v}_k^l.$$
$$\triangleq h\left(\boldsymbol{x}_k, z_k^l, s_k^l, \boldsymbol{v}_k^l\right) \qquad (A4)$$

REFERENCES

[1] H. Zhu, H. Leung, and K. V. Yuen, "A joint data association, registration, and fusion approach for distributed tracking," *Inf. Sci.*, vol. 324, pp. 186–196, Oct. 2015, doi: 10.1016/j.ins.2015.06.042.

[2] Y. Cao, G. Wang, D. Yan, and Z. Zhao, "Two algorithms for the detection and tracking of moving vehicle targets in aerial infrared image sequences," *Remote Sens.*, vol. 8, no. 1, p. 28, Dec. 2015, doi: 10.3390/rs8010028.

[3] F. Lian, G.-H. Zhang, Z.-S. Duan, and C.-Z. Han, "Multi-target joint detection and estimation error bound for the sensor with clutter and missed detection," *Sensors*, vol. 16, no. 2, p. 169, Jan. 2016, doi: 10.3390/s16020169.

[4] J. Liu, F. Lian, and M. Mallick, "Distributed compressed sensing based joint detection and tracking for multistatic radar system," *Inf. Sci.*, vol. 369, pp. 100–118, Nov. 2016, doi: 10.1016/j.ins.2016.06.032.

[5] W. Liu and Z. Gao, "A distributed flocking control strategy for UAV groups," *Comput. Commun.*, vol. 153, pp. 95–101, Mar. 2020, doi: 10.1016/j.comcom.2020.01.076.

[6] Z. Chen, B. Zhong, G. Li, S. Zhang, R. Ji, Z. Tang, and X. Li, "SiamBAN: Target-aware tracking with Siamese box adaptive network," *IEEE Trans. Pattern Anal. Mach. Intell.*, vol. 45, no. 4, pp. 5158–5173, Apr. 2022, doi: 10.1109/TPAMI.2022.3195759.

[7] Y. Zheng, B. Zhong, Q. Liang, Z. Tang, R. Ji, and X. Li, "Leveraging local and global cues for visual tracking via parallel interaction network," *IEEE Trans. Circuits Syst. Video Technol.*, early access, Oct. 10, 2022, doi: 10.1109/TCSVT.2022.3212987.

[8] K. Da, T. Li, Y. Zhu, H. Fan, and Q. Fu, "Recent advances in multisensor multitarget tracking using random finite set," *Frontiers Inf. Technol. Electron. Eng.*, vol. 22, no. 1, pp. 5–24, Jan. 2021, doi: 10.1631/FITEE.2000266.

[9] R. R. Sanaga and C. Frueh, "Probability hypothesis density filter with uncertainty in the probability of detection," *Adv. Space Res.*, vol. 67, no. 5, pp. 1437–1453, Mar. 2021, doi: 10.1016/j.asr.2020.11.035.

[10] G. Li, G. Li, and Y. He, "Distributed GGIW-CPHD-based extended target tracking over a sensor network," *IEEE Signal Process. Lett.*, vol. 29, pp. 842–846, 2022, doi: 10.1109/LSP.2022.3158589.

[11] Q. Luo, Z. Gao, and C. Xie, "Improved GM-PHD filter based on threshold separation clusterer for space-based starry-sky background weak point target tracking," *Digit. Signal Process.*, vol. 103, Aug. 2020, Art. no. 102766, doi: 10.1016/j.dsp.2020.102766.

[12] Z. Zhang, J. Sun, H. Zhou, and C. Xu, "Group target tracking based on MS-MeMBer filters," *Remote Sens.*, vol. 13, no. 10, p. 1920, May 2021, doi: 10.3390/rs13101920.

[13] C.-T. Do, T. T. D. Nguyen, and H. V. Nguyen, "Robust multi-sensor generalized labeled multi-Bernoulli filter," *Signal Process.*, vol. 192, Mar. 2022, Art. no. 108368, doi: 10.1016/j.sigpro.2021.108368.

[14] C.-T. Do, T. T. Dat Nguyen, D. Moratuwage, C. Shim, and Y. D. Chung, "Multi-object tracking with an adaptive generalized labeled multi-Bernoulli filter," *Signal Process.*, vol. 196, Jul. 2022, Art. no. 108532, doi: 10.1016/j.sigpro.2022.108532.

[15] X. Xue, S. Huang, J. Xie, J. Ma, and N. Li, "Resolvable cluster target tracking based on the DBSCAN clustering algorithm and labeled RFS," *IEEE Access*, vol. 9, pp. 43364–43377, 2021, doi: 10.1109/ACCESS.2021.3066629.

[16] Z. Liang, F. Liu, L. Li, and J. Gao, "Improved generalized labeled multi-Bernoulli filter for non-ellipsoidal extended targets or group targets tracking based on random sub-matrices," *Digit. Signal Process.*, vol. 99, Apr. 2020, Art. no. 102669, doi: 10.1016/j.dsp.2020.102669.

[17] M. Barbary and M. H. A. El-Azeem, "Track-before-detect for complex extended targets based sequential Monte Carlo Mb-sub-random matrices filter," *Multidimensional Syst. Signal Process.*, vol. 32, no. 3, pp. 863–896, Jul. 2021, doi: 10.1007/s11045-021-00762-3.

[18] M. Baum and U. D. Hanebeck, "Extended object tracking with random hypersurface models," *IEEE Trans. Aerosp. Electron. Syst.*, vol. 50, no. 1, pp. 149–159, Jan. 2014, doi: 10.1109/TAES.2013.120107.

[19] L. Sun, H. Yu, J. Lan, Z. Fu, Z. He, and J. Pu, "Tracking of multiple maneuvering random hypersurface extended objects using high resolution sensors," *Remote Sens.*, vol. 13, no. 15, p. 2963, Jul. 2021, doi: 10.3390/rs13152963.

[20] K. Granström and U. Orguner, "A PHD filter for tracking multiple extended targets using random matrices," *IEEE Trans. Signal Process.*, vol. 60, no. 11, pp. 5657–5671, Nov. 2012, doi: 10.1109/TSP.2012.2212888.

[21] D. Schuhmacher, B.-T. Vo, and B.-N. Vo, "A consistent metric for performance evaluation of multi-object filters," *IEEE Trans. Signal Process.*, vol. 56, no. 8, pp. 3447–3457, Aug. 2008, doi: 10.1109/TSP.2008.920469.

[22] C. Han, "Research on multi-extended target tracking based on random hypersurface model and performance evaluation index," M.S. thesis, Xidian Univ., Xi'an, China, 2019.

[23] H. Peng, G. Huang, W. Tian, and H. Qiu, "δ-GLMB filter based on DI in a clutter," *J. Eng.*, vol. 2019, no. 20, pp. 7000–7005, Oct. 2019, doi: 10.1049/joe.2019.0471.

[24] M. Xiaohui, Y. Fengbao, L. Zhe, T. Xiaowei, and Z. Yaling, "Delta-GLMB filter multi-target tracking algorithm based on square-rooted cubature Kalman," *Comput. Appl. Softw.*, vol. 37, no. 4, pp. 164–170, 2020.

[25] L. Wang, R. Zhan, S. Liu, J. Zhang, and Z. Zhuang, "Joint tracking and classification of multiple extended targets via the PHD filter and star-convex RHM," *Digit. Signal Process.*, vol. 111, Apr. 2021, Art. no. 102961, doi: 10.1016/j.dsp.2020.102961.

[26] Z. Liang, F. Liu, and J. Gao, "Improved GGIW-PHD filter for maneuvering non-ellipsoidal extended targets or group targets tracking based on sub-random matrices," *PLoS ONE*, vol. 13, no. 2, Feb. 2018, Art. no. e0192473, doi: 10.1371/journal.pone.0192473.

YIJIN WANG was born in Shanxi, China, in 1994. He received the M.S. degree in electronics science and technology from Air Force Engineering University, Xi'an, China, in 2019. He is currently pursuing the Ph.D. degree. His research interests include microwave remote sensing, SAR imaging, computational electromagnetism, and target detection.

CHUANGMING TONG was born in Hubei, China, in 1964. He received the M.S. and Ph.D. degrees in electromagnetic field and microwave technology from Air Force Missile College, in 1988 and 1999, respectively. From 1999 to 2002, he was a Visiting Scholar with the State Key Laboratory of Millimeter Waves, Southeast University, Nanjing, China. He is currently a Professor and a Doctoral Supervisor with Air and Missile Defense College, Air Force Engineering University. His research interests include microwave remote sensing, computational electromagnetism, and target tracking.

JIAHAO XIE was born in 1996. He received the bachelor's degree from the School of Mechanical Engineering, Hebei University of Technology, Tianjin, China, in 2017, and the master's and Ph.D. degrees from Air and Missile Defense College, Air Force Engineering University, Xi'an, Shaanxi, China, in 2019 and 2022, respectively. Currently, he is with Space Engineering University as a Lecturer. His research interests include multiobjective tracking and information fusion.

• • •